Using a discrete element method to investigate seismic response and spin change of 99942 Apophis during its 2029 tidal encounter with Earth

Joseph V. DeMartini[a,*], Derek C. Richardson[a], Olivier S. Barnouin[b], Nicholas C. Schmerr[a], Jeffrey B. Plescia[b], Petr Scheirich[c], Petr Pravec[c]

[a] *University of Maryland, United States of America*
[b] *John's Hopkins Applied Physics Lab, United States of America*
[c] *Academy of Sciences of the Czech Republic, Czech Republic*

ABSTRACT

Near-Earth Asteroid 99942 Apophis presents a unique opportunity to study the dynamics, bulk properties, and interior structure of a rubble-pile asteroid when it makes its close encounter with the Earth in 2029. In order to better understand the potential outcomes of a tidal encounter between Earth and Apophis, and to support a potential future mission to Apophis, we perform numerical simulations of the encounter. We represent Earth as a single rigid sphere and the target body as a cohesionless, self-gravitating granular aggregate of identical spheres in a hexagonal-close-packed configuration subject only to gravitational and soft-sphere (elastic) contact forces. We use a radar-derived shape model for the asteroid, along with current best estimates for the orbital solution of Apophis to simulate the encounter trajectory, and perform a large parameter sweep over different potential encounter orientations and bulk densities for the body. We find that the median change in the rotational period for Apophis, sampled for a range of different initial body and spin orientations, is $-1.9\,\mathrm{h}$ (mean -0.1 ± 6.0 (1-σ) hours) during the encounter. Additionally, we measure that the mean of the largest change in axis length among the 3 primary body axes, also sampled over trials with different initial body and spin orientations, is $0.132 \pm 0.066\,\mathrm{mm}$ during the encounter, assuming a bulk Young's Modulus of $10^6\,\mathrm{Pa}$. Such strains on the timescale of peak stress during the encounter may be large enough to be detected by an in-situ seismometer.

1. Introduction

Discovered in 2004, asteroid 99942 Apophis (formerly 2004 MN₄) is a Near-Earth Asteroid (NEA) that is among the population of Potentially Hazardous Asteroids (PHAs). When it was discovered, Apophis was originally estimated to have over a 2% chance of impacting the Earth in 2029 (Farnocchia et al., 2013). Follow-up measurements and historical data reduced the impact risk significantly, and we now know that, on April 13, 2029, Apophis will miss the Earth, but come within 5.7 ± 1.4 Earth radii (3-σ uncertainty) of our planet's center (Brozović et al., 2018). This close encounter with Apophis, whose diameter is close to 400 m (Brozović et al., 2018), provides an excellent opportunity to study the properties of sub-kilometer-diameter asteroids.

If Apophis is like the only other well-studied asteroid in its size category to date 25143 Itokawa (Abe et al., 2006), the body is most likely a rubble pile or a gravitational aggregate of smaller blocks, possibly with a surface layer of granular material and with constituent particle sizes ranging from silts to gravels to boulders (Richardson et al.,

2002; Fujiwara et al., 2006; Saito et al., 2006; Miyamoto et al., 2007; Barnouin-Jha et al., 2008). Apophis' perigee distance is not small enough for Earth's tidal forces to disaggregate the body, but may be small enough to trigger detectable changes in surface morphology (Yu et al., 2014; Binzel et al., 2010) and spin state (Richardson et al., 1998; Scheeres et al., 2000, 2005; Scheeres, 2001), and produce measurable seismic activity. Knowing about this close encounter well in advance of its occurrence provides a unique opportunity for scientists to prepare missions and studies that are usually not possible due to lack of warning. Measurements of the amount of void space in Apophis, and thus how well seismic signals propagate through the body, can reveal a great deal about the internal structure of rubble-pile bodies, which can be an important factor in determining the effectiveness of mitigation techniques such as kinetic impactors. The 2029 tidal encounter between Earth and Apophis therefore provides an exciting opportunity to not only to improve our understanding of rubble-pile asteroids, but to inform future decisions regarding impact risk and mitigation.

* Corresponding author.
 E-mail address: jdema@astro.umd.edu (J.V. DeMartini).

1.1. Simulating tidal encounters

Previous numerical work studying the tidal evolution of objects in close proximity includes methods treating the bodies as fluids (e.g., Press and Teukolsky, 1977). More recently, tidal evolution of rubble-pile asteroids has been studied by Richardson et al. (1998), Walsh and Richardson (2008), Walsh and Richardson (2012), and Yu et al. (2014), who used N-body gravity codes with a treatment of collisions to model the disruptive effects of close tidal encounters with Earth. Here, we take the same approach, using the most recent version of the N-body gravity code, *pkdgrav*, which treats the collisional interactions of both flowing and quasi-static granular materials very accurately using a soft-sphere discrete element method (SSDEM), appropriate for very weak tidal encounters where individual components remain in persistent contact for much if not all of the duration. The code and numerical approach are described more fully in Section 2.1.

1.2. Apophis shape models

The most comprehensive analyses of the shape of Apophis were performed by Brozović et al. (2018) and Pravec et al. (2014). In this study, we use the most recent shape model, published in Brozović et al. (2018), based on radar observations from the Goldstone Observatory in California and the Arecibo Observatory in Puerto Rico. The updated shape model constrains the lower bound on the major axis of the body to be 450 m and accounts for possible concavities that the earlier, convex shape model could not. Furthermore, the newer best-fit shape model for Apophis shows that the body may be a contact binary (see Fig. 1) but the authors caution that there is still a significant degree of uncertainty in the newer shape model, as the radar images did not have enough resolution to make a high-fidelity model.

Beyond putting constraints on the shape of Apophis, the 2018 analysis also further refines the orbital path of the body. This refined orbit was used to update the ephemerides in the JPL Horizons database, which we use in this study. The main uncertainty in the orbital path of the body, however, is the Yarkovsky effect; current observational data is not precise enough to constrain the magnitude of the Yarkovsky effect on the orbit of Apophis (Brozović et al., 2018). It is estimated that future radar observations of Apophis in 2021 and during the 2029 close encounter will better constrain the strength of the Yarkovsky effect, further improving the accuracy of the orbital solution of Apophis. Knowing how Yarkovsky forces affect the asteroid will likely lead to more precise estimates of its mass and bulk density (see Section 2.2.3), which will in turn provide information about the internal structure of the body.

1.3. Apophis spin state

The current best estimates for the spin state of Apophis come from Pravec et al. (2014). Apophis is understood to have a 27.38 ± 0.07 h non-principal axis rotation period for the major axis precession about the angular momentum vector and a 262 ± 6 h rotational period about the major axis. This precession and rotation combine to give an overall retrograde rotational period of 30.56 ± 0.01 h, so Apophis is classified

as a slowly tumbling body. The complex tumbling motion and long period of Apophis make it difficult to determine the body's orientation at the time of encounter. This issue is not helped by the large uncertainties on the angular momentum vector of the body (shown by the shaded region in Fig. 4 of Pravec et al., 2014), which is nominally placed at ecliptic longitude and latitude 250° and −75° respectively. In this analysis, we will use initial body and spin orientations derived from this nominal solution as described in Section 2.2.

1.4. Application to possible future mission

The motivation for the simulations of the 2029 Apophis close encounter performed here is as a proof-of-concept for any future mission to visit this asteroid during the 2029 encounter. Such a mission might arrive several months before perigee, place a seismometer on the body, and use seismological and observational data around the time of encounter to fully characterize the tidal effects on Apophis' exterior and interior. Such processes are believed to be important for the structural evolution of asteroids, but are not well characterized. Furthermore, such a mission would put constraints on the rotational state, bulk properties, interior structure, and geological history of Apophis. Using natural micrometeorite sources to gauge the background signal, a mission with seismometers would have the potential to gain significant insight about the interior nature of Apophis from this tidal encounter. Taken together, these measurements will help mitigation strategies (e.g., the effectiveness of a kinetic impactor) for this and similar bodies.

1.5. Study outline

In this study, we model Apophis as a cohesionless, self-gravitating rubble pile. We investigate the tidal effects of the Earth on the asteroid as Apophis passes by during its 2029 close encounter, performing a wide sweep over the uncertainties in bulk density, orientation, and spin state in order to assess the plausible range of effects from the encounter as a function of assumed material parameters. We track tidal stresses by monitoring the lengths of the principal axes of the body across the simulations, and we measure the change in the overall rotational state as well. Section 2 describes the numerical approach in greater detail. Results of the study are presented in Section 3. We discuss the implications of the results and provide a summary in Sections 4 and 5, and mention ideas for future work on this topic in Section 6.

2. Methodology

2.1. Soft sphere discrete element method (SSDEM)

We model Apophis as a rubble pile using the parallelized N-body gravity tree code *pkdgrav* (Richardon et al., 2000; Stadel, 2001). The body is represented by a collection of gravitationally interacting spheres in contact with one another, with interparticle friction and deformation modeled with a soft-sphere discrete element method (SSDEM; Schwartz et al., 2012; Sánchez and Scheeres, 2011). The SSDEM implementation uses tiny overlaps between the particles at the point of contact as a proxy for surface deformation, using a repulsive,
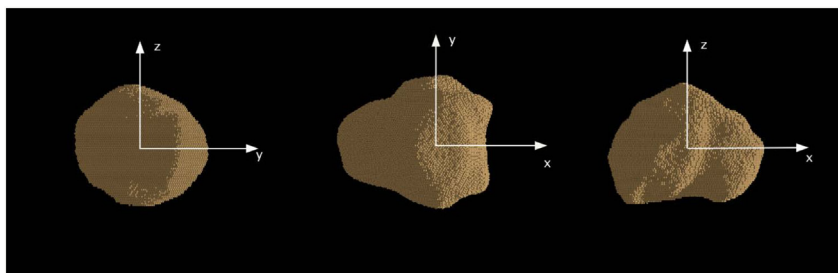

Fig. 1. Three views of the Brozović et al. (2018) model of Apophis, as created from a *pkdgrav* hexagonal-close-packing of monodisperse particles (see Section 2.2.1). In this figure, the x-direction points along the major axis of the body, the y-direction along the intermediate axis, and the z-direction along the minor axis. Note, in the rightmost image, the possible contact-binary nature of the object, which is a result of the new best-fit shape for Apophis (Brozović et al., 2018).

Table 1
Definitions of simulation parameters.

Quantity	Symbol	Value/Range
Perigee Distance	q	$5.96\ R_{\oplus}$
Speed at Perigee	v_q	7.43 km/s
Bulk Rotation Period	P	30.56 h
Coefficient of Static Friction	μ_s	1.0
Coefficient of Rolling Friction	μ_r	1.05
Coefficient of Twisting Friction	μ_t	1.3
Shape Parameter	β	0.5
Coefficient of Restitution (Normal)	ϵ_n	0.55
Coefficient of Restitution (Tangential)	ϵ_t	0.55
Bulk Density	ρ_B	1.1–3.6 g/cm^{-3}
Young's Modulus	Y	1–10^3 kPa
Particle Number (Resolution)	N	10^2–10^4
Particle Radius (at $N = 10^4$)	R	7.18 m
Particle Mass (at $N = 10^4$)	m_p	$(2.3 - 7.5) \times 10^6$ kg
Spring Constant (Normal)	k_n	– (varies)
Timestep	δ	– (varies)

Hooke's Law spring force with a linear spring constant calculated so that the particles do not exceed some nominal overlap fraction (generally 1% of the smallest particle radius, but in our case we take a different approach — see Section 2.2), and calculates the forces and torques due to the overlaps with neighboring particles. The approach also accounts for normal and tangential damping derived from restitution coefficients, along with sliding and static friction, where dissipation arises due to dynamical sliding friction above the static threshold (Schwartz et al., 2012). Also, using a particle shape parameter coupled with the friction coefficients, we model rolling and twisting friction (Zhang et al., 2017).

The equations of motion in *pkdgrav*, which, for this scenario, consist of the mutual gravitational and collisionally induced accelerations of discrete particles, are solved using a second-order leapfrog method. The SSDEM approach used in *pkdgrav* has been validated through comparisons with laboratory experiments (e.g., Schwartz, 2013). In addition, *pkdgrav* has been used to study the dynamics of granular systems and rubble-pile asteroids, including investigations of avalanches on Apophis (Yu et al., 2014), constraints on the internal structure of fast-rotating asteroid 65803 Didymos (Zhang et al., 2017), and simulations of the impact of the MASCOT lander deployed by Hayabusa2 on 162173 Ryugu (Thuillet et al., 2018).

2.2. Simulation preparation

2.2.1. Rubble-pile construction

The rubble-pile model of Apophis used in these simulations is constructed by carving out the radar-derived shape model of Brozović et al. (2018) from a collection of monodisperse, equal-density spheres. For the simulations conducted here, particles have radii of 7.14 m, such that the final body contains a total number of particles $N \approx 10{,}000$.

The body from which we carve the final shape is created by generating a hexagonal-close-packed (HCP), approximately spherical distribution of particles in a volume with axis lengths no smaller than the maximum axis length of Apophis and containing substantially $> 10{,}000$ particles. Using HCP significantly lowers the amount of void space between the particles and shortens the amount of time that the body needs to equilibrate dynamically, however, we note that force chains in HCP configurations are not isotropic (Quillen et al., 2016), which could result in some artificial enhancement of shear strength. After the spherical distribution is created, the shape model from Brozović et al. (2018) is carved out of the larger aggregate. Due to the introduction of a bulk spin (see Section 2.2.3), the newly carved body is allowed to settle under its own gravity and initial spin state until it reaches equilibrium. We define equilibrium as a state in which the interparticle restoring spring force (defined in Section 2.1) and the interparticle gravity force are nearly equal. The competing spring force and

gravitational forces cause the overlapping particles to oscillate slightly; we measure equilibrium by finding the point at which the amplitude of the oscillations is $< 1\%$ of the maximum axis length change that we expect to see during encounter. We have calibrated that, for a bulk density of 2.9 g/cm^{-3} and under one random initial spin state, it takes any of our models approximately 2 h of simulated time in free space to reach the equilibrium that we have defined, at which point it is ready for the encounter. We use this same amount of simulated settling time before every encounter simulation. For encounters simulated using a model with a different bulk density but equivalent spring constant, we estimate that the amount of settling time required for the body to reach equilibrium scales like the inverse square-root of the particle mass, as per the canonical harmonic oscillator frequency.

2.2.2. Rubble pile parameters

In the simulations conducted here, we use nominal friction and restitution parameters equivalent to those used in Zhang et al. (2017) for 65803 Didymos, another likely rubble-pile asteroid with diameter < 1 km. The coefficient of sliding friction $\mu_s = 1.0$ and the shape parameter $\beta = 0.5$, where higher β represents more angular particles (Zhang et al., 2017). These μ_s and β values, along with our adopted rolling ($\mu_r = 1.05$) and twisting ($\mu_t = 1.3$) friction coefficients, are representative of material with friction angle comparable to that of terrestrial sands. Normal and tangential restitution coefficients (ϵ_n and ϵ_t, respectively) are both set to 0.55, within the range of restitution parameters for terrestrial rocks (Chau et al., 2002). In any case, we note that terrestrial analogs are likely not identical to the material on the surfaces of rubble piles, but represent a reasonable estimate for what the material parameters may be like for these bodies. We summarize these values, along with other simulation parameters, in Table 1.

While the normal spring constant used in SSDEM, k_n, and timestep, δ, are most often chosen for numerical convenience such that particles do not overlap $> 1\%$ of the smallest particle radius, we find that in this case where we do not expect adjacent particles to come out of contact, the value of the spring constant that we use has a significant effect on the stresses that we measure. Rigid materials such as gravels/boulders would never overlap or deform by as much 1% in equilibrium contact except under extreme pressure. If particles are not coming out of contact, then a spring constant that is too soft would overestimate the amount of tidal strain that is observed across an encounter. To address this issue, we adopt a more physically motivated approximation for the spring constant based on the Young's modulus of the assumed material, which is defined as the ratio of stress to strain along a given axis for a material, with units of pressure. We estimate k_n for a given Young's modulus Y from Hooke's Law assuming the force acts over the cross-sectional area of a typical particle of radius R, giving,

$$k_n \sim \pi R Y. \tag{1}$$

We do not know the component material for Apophis, but we have already assumed that Apophis is a rubble pile with a range of block and grain sizes likely similar to Itokawa and comet 67P/Churyumov-Gerasimenko. Based on these considerations, we choose a representative number for the Young's modulus of 1 MPa to use in the bulk of our simulations, a value in the region of that found for comet 67P (Möhlmann et al., 2017) and characteristic of low-density (porous) silts/gravels on Earth.[1] This Young's modulus corresponds to a normal spring constant $k_n = 2.26 \times 10^7$ N/m from Eq. (1) and requires a timestep $\delta = 0.039$ s to sufficiently sample the full spring cycle (Schwartz et al., 2012). These values are treated as a fixed material property and are thus identical in all simulations, regardless of changes

---

[1] http://www.geotechdata.info/parameter/soil-young's-modulus.html — note that experiments on Earth are usually not conducted using perfectly dry materials, nor in vacuum, nor in low gravity. The values we adopt are used for guidance.

to bulk density or initial spin orientation. The timestep and spring constant do, however, change slightly in trials using different particle resolution, as changes to the typical particle radius are directly proportional to changes in k_n for the same Young's modulus. We also examine a small number of cases where we change the Young's modulus of the material to determine the effects of different material strengths on the tidal stretching (see Section 2.2.3).

2.2.3. Variable initial conditions

Prior to beginning the encounter, we settle Apophis under one of over 4000 spin states generated within the uncertainties of the nominal solution found in Pravec et al. (2014). The spin states were generated by integrating the non-principal-axis rotational motion of Apophis for 11 years (2013 to 2023) and choosing one orientation for each day at a random time within the day. The interval does not include 2029, but we simulate 32 non-repeating initial spin states randomly selected from the list at constant bulk density, $\rho \approx 2.9\,\mathrm{g/cm}^{-3}$, in order to put constraints on the possible outcomes given a range of plausible orientations at perigee. We apply these spin states by imposing the randomly chosen spin vector on the body, thus neglecting the tumbling motion of the body in favor of a single mean spin. This approach assumes that the non-principal axis motion of the body has a negligible effect over the encounter, as the mean spin period $(30.56 \pm 0.01\,\mathrm{h})$ is close to the precession period, but the rotation period is almost ten times longer (Pravec et al., 2014), and the encounter timescale is less than both, falling at about $10\,\mathrm{h}$ (Fig. 2). In other words, by using the mean as the actual spin of Apophis, we are neglecting the effects of varying centrifugal forces on the body. We show in B that, to first order, the difference in the largest centrifugal acceleration on the body (if the spin period were exactly equal to the precession period) and the centrifugal acceleration from the mean spin is a few percent of the tidal acceleration felt at perigee, and therefore we may neglect its effects. We use

(a) Timeline

(b) Trajectory

Fig. 2. (a) A timeline of the encounter simulation (excluding settling time) showing the intervals before, during, and after encounter, as well as the region of maximum signal strength, labeled Perigee. (b) Trajectory of Apophis during the encounter simulation in the geocentric equatorial coordinate system. The dashed line represents the period in which Apophis is below the Earth's equator (negative z-value) and the solid line shows the period in which Apophis is above the Earth's equator. Encounter start, end, and maximum (perigee), as defined in Fig. 2a are noted with green, red, and black dots respectively. (For interpretation of the references to color in this figure legend, the reader is referred to the web version of this article.)

$2.9\,\mathrm{g\,cm}^{-3}$ for the bulk density in these spin tests as it lies close to the middle of the range of bulk densities that we also test at fixed spin (discussed next) but errs on the conservative side, since we expect a higher bulk density to lead to a smaller measured strain signal.

We also investigate six different bulk densities for Apophis, ranging from $1.1\,\mathrm{g/cm}^{-3}$ to $3.6\,\mathrm{g/cm}^{-3}$ in steps of $0.5\,\mathrm{g/cm}^{-3}$, at one fixed but arbitrary initial spin state. We indicate this range and the other variable ranges that we investigate in Table 1. The range of bulk densities that we test encompasses plausible bulk densities for rubble-pile bodies, based on measurements of LL-chondrite meteorite samples (to which Apophis is likely similar in composition), on the high end (Binzel et al., 2009) and Itokawa on the low end (Abe et al., 2006). We adjust the bulk density of the body not by changing porosity but by uniformly increasing or decreasing particle masses while keeping their radii fixed. In reality, the densities of each of the constituent grains that make up Apophis will all be in the region of 3.1 to $3.8\,\mathrm{g/cm}^{-3}$ (Flynn et al., 1999; Britt et al., 2002). By changing particle masses to adjust the overall bulk density, the equilibrium positions of the particles actually change: interparticle gravity pulls them closer together as their mass increases. This results in a small, but relevant, change in the shape of the different models of Apophis for each different bulk density, thus changing the inertia tensor of the body, and therefore its spin state. What this means is that bodies with different bulk densities but the same initial spin state will have a slightly different orientation at perigee. Some of the variability in strain signals measured from density variations will therefore be effects that we are trying to measure separately in the variable spin state simulations discussed above. To determine the importance of these influences, we perform the set of simulations at each different density with 3 separate fixed initial spin states. This helps to discern which effects are caused by the varying density and which are caused by varying spin state. For these tests, we are interested in establishing the range of strain outcomes for a fixed initial spin state, since lower-density bodies ought to experience a greater strain for the same tidal stress, in accordance with the Roche limit.

We also investigate 4 different values for the Young's modulus (modeled by our spring constant k_n) ranging from 1 kPa to 1 MPa by factors of 10, in order to discern how the strain signal scales with the effective material strength of the body. We postulate that the signal will be stronger for a smaller Young's modulus because the individual grains will be more easily deformed. Importantly, by determining a trend in how the Young's modulus affects the measured strains on Apophis during the encounter, we can scale our measurements once the actual Young's modulus is known. We equilibrate all of the bodies in this suite of simulations for the same length of simulated time, bounded by the model with the lowest Young's modulus (the longest equilibration time), to ensure that they all experience the encounter at as close as possible to the same spin orientation. We note that, similar to the situation above where changing the bulk density caused a change in the overall body shape and thus the inertia tensor describing the body, changing the Young's Modulus will cause an overall change in shape, and thus influence the encounter orientation. Where before we estimate that the change signal strength with encounter orientation is important with regard to differences in bulk density, we estimate that the change in signal strength due to the changing Young's Modulus will drown out the changes due to encounter orientation (see Fig. 9).

In conjunction with these measurements of Young's modulus, we investigate the effects of particle resolution on the measured strain during encounter. We investigate models with particle number N ranging from 100 to 10,000 by factors of 10. For each of these models, we examine all 4 values of Young's modulus described above using the same initial spin orientation in each encounter. The expectation is that a lower-resolution model of Apophis experiences a greater strain signal at each value of Young's modulus, because interparticle gravity will be weaker due to larger-radius particles having larger particle center separations. Results for these and all other simulations are described in
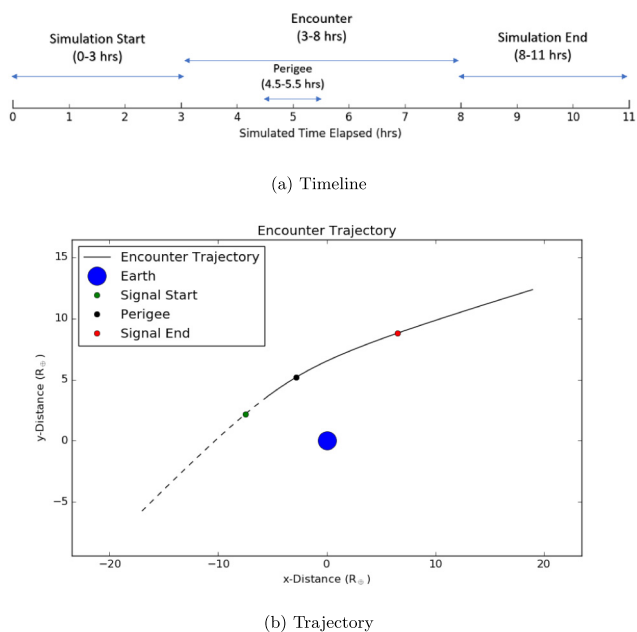
Section 3.

2.3. Tidal stressing

We test our procedure by calculating and simulating the amount of expected tidal stress experienced by two identical particles with their center of mass in the same location as that expected of Apophis at closest approach and oriented such that the tidal force at perigee is maximized. Short simulations of this two-particle system in equilibrium in free space versus equilibrium at perigee, using the same simulation parameters as described in Section 2.2, show a change in particle separation approximately equal to 1 μm. This result is confirmed by analytical calculations using the first-order approximation of the tidal force of the Earth on the particles (A). Extrapolating this to the scale of the full asteroid, we expect that the body will experience strains on the scale of tens of microns. This amount of tidal strain is not enough to separate grains that are in contact. Rather, it is best to think of the strain as a rigid body deformation: grains in contact will not be sliding past one another, but rather flexing or "breathing" individually across the entire body, implying that interparticle friction should not play a large role in the signal measured. This estimate agrees with the classification of the Apophis encounter according to Richardson et al. (1998) in their Fig. 4 as an *N*-type, meaning no major change during the encounter. That earlier work, however, did not have a sufficiently accurate treatment of granular physics to measure the small changes that we investigate in this paper. The overall effect on the body will be small, but the motion could be detectable by an in-situ seismometer (Schmerr et al., 2018; see Section 4).

2.4. Encounter details

As described in Section 2.2.1, each simulation is begun by settling the rubble-pile model of Apophis under its own gravity and spin in free space, with the bulk density and randomized initial spin state chosen as detailed above. During the settling period, Apophis is subject only to its own interparticle gravity and contact forces, and the simulation time spans a sufficient interval for the body to fully equilibrate (generally ∼2 h of simulated time), with the equilibrium condition described above (Section 2.2.1).

Once Apophis is settled, we put the body barycenter at the origin and add a single particle with mass and relative position and velocity representative of the Earth in the simulation. The initial conditions for the encounter are taken from the hourly geocentric ephemeris of Apophis from the JPL Horizons Database,[2] as updated on August 2017 with the most recent radar data from Brozović et al. (2018). We begin the encounter 5 h prior to close approach and end 6 h after, for a total simulated time of 11 h per encounter (see Fig. 2 for details). We choose these starting and ending times because preliminary trials showed that the strains felt on Apophis were minimal from times about 3 h before and after close approach; we then choose to allow for an extra 2–3 h of time beyond that, so that we can accurately measure the tails of the trends in the encounter during our analysis, as well as to ensure full equilibrium before encounter. The encounter takes place in the Apophis frame, such that Apophis remains at rest (except for its rotation) at the origin to reduce round-off error. The Earth particle has motion such that the initial position and velocity are equal and opposite to the positions and velocities given in the ephemeris for Apophis relative to Earth at 5 h prior to perigee.

We model the Earth as a single rigid sphere, as we are mainly concerned with the first-order effects of the Earth's perturbation on the asteroid at close approach. To this end, the inclination of Apophis' orbit with respect to the Earth's equator, the Earth's oblateness, and the positions of the Moon and Sun with respect to the target body are not

simulated. While the Sun and Moon positions may have small effects on the strain and spin change experienced by Apophis, we expect that these effects will be negligible both on the encounter timescale and in comparison to the effect of the first-order tidal stress from the Earth, but may be investigated in future work. Furthermore, the effect of the Earth's oblateness (< 1%) on the spin pole is insignificant in comparison to the current uncertainties on the rotational phase and spin orientation.

3. Simulation results

3.1. Runs performed & analysis methods

For each encounter, we characterize the maximum strain by determining the maximum change in axis length for each of the three principal axes. We use tagged particles at the ends of the major, minor, and intermediate axes and track the distance between the centers of these particles to determine which body axis experiences the maximum strain during the encounter. Note that, due to the coarse nature of this model, these particles may not lie exactly along the principal axes, but they will always be close. Also note that the maximum strain may not always occur along the principal axes (although these axes will generally be most susceptible), which is partly why we also track changes in axis length between seven random pairs of particles in the bodies. These random pairs of particles are not constrained to lie just on the surface of the body, so by tracking the change in their separations, we can identify how the strength of the signal (that is, the stresses and strains across the asteroid) changes in the interior of the body and along arbitrary axes when compared to the changes along the principal body axes. In determining the change in the spin state of Apophis during the encounter, we measure the difference between the initial and final bulk spin periods of the body, to determine an increase or decrease.

3.2. Dependence on variable initial spin orientations

3.2.1. Axis length change

Fig. 3 shows an example of the strains measured across Apophis over the course of the nominal 2029 encounter trajectory. The typical encounter timescale, constituting significant changes in axis length or spin period, lasts approximately 5 h. In the figure, and over the course of these 5 h, one can clearly see the body axes go through stages of tension (black line showing the minor axis), compression (blue line, intermediate axis), or both (pink line, a random axis), depending on the orientation of the axis during close approach. These behaviors are seen along the segments separating the randomly selected fiducial particle pairs at typically smaller amplitudes than along the primary body axes. (For interpretation of the references to color in this section, the reader is referred to the web version of this article.)

Table 2 summarizes results for the 32 simulations with the same density (2.9 g/cm^{-3}) but differing initial spin states. Fig. 4 provides a visual summary of the data for axis length change. Note for this table and figure, only the maximum length change measured among the 3 principal axes in any given run was used. From these data, we see that a typical maximum axis length change is approximately 0.130 mm for these initial conditions, and that the range of encounter orientations can result in (sometimes very large) increases or decreases to the asteroid's rotation period, or have little effect at all.

3.2.2. Period change

Fig. 5 shows a nominal example, from the same run as in Fig. 3, of the change in the spin frequency (the inverse of the spin period) of Apophis over the course of the tidal encounter. We note that the magnitude of the angular momentum is proportional to the magnitude of the spin frequency due to the near-constancy of the inertia tensor throughout the encounter; we calculate the angular momentum

---

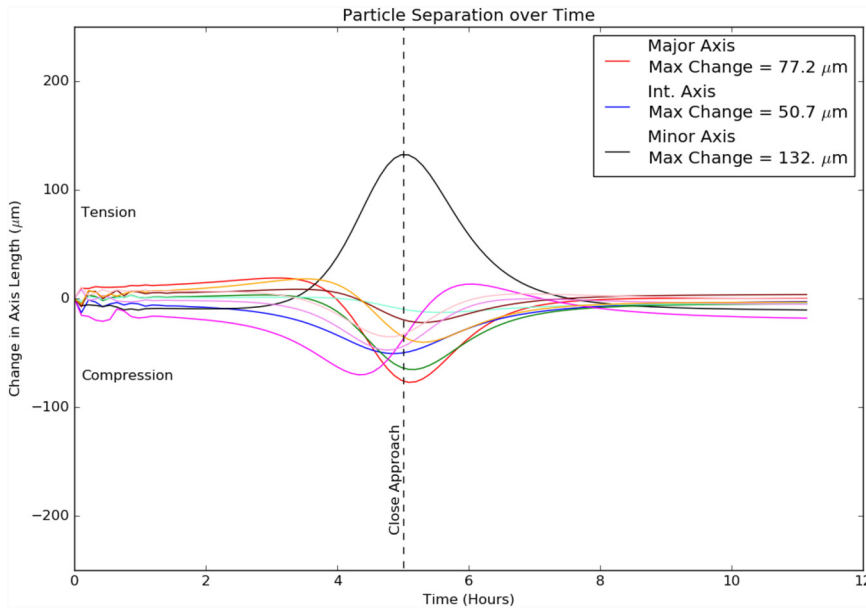[2] https://ssd.jpl.nasa.gov/horizons.cgi.

Fig. 3. Plot of the changes in the lengths of the 3 principal axes and 7 random segments in Apophis. The maximum measured strains along the primary body axes are given in the legend, in microns, as determined by the method described in Section 3.1. Positive axis length changes show particles under tension (being pulled apart) while negative axis length changes show compression (being pushed together); the regions of tension and compression are marked on the left side of the figure. The dashed vertical line marks the point 5 h after the start of the simulation, at the time that Apophis reaches perigee; note that this is also the time at which most axes experience maximum tension or compression. Transients seen at the start of the encounter (left side of the image) along some of the axes are remnants of the settling process. These transients have amplitudes well below that of the signal measured at perigee and are generally damped before the encounter signal begins. (For interpretation of the references to color in this figure, the reader is referred to the web version of this article.)

Table 2

Outcome statistics for 32 Apophis encounter simulations with constant bulk density and varying initial spin state (corresponding histograms of the axis length and spin changes are shown in Figs. 4 and 6, respectively).

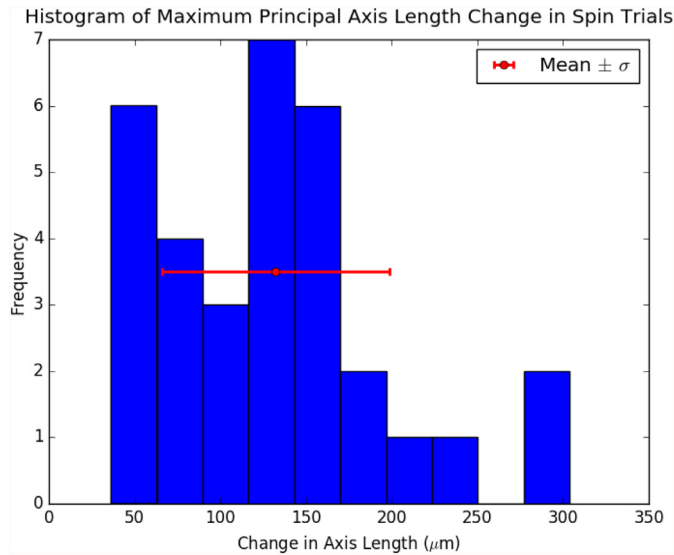| Quantity measured	Max.	Min.	Mean	Median	St. Dev.
Length change (mm)	0.3038	0.0363	0.1322	0.1297	0.0663
Period change (h)	14.440	−7.603	−0.065	−1.854	6.028

Fig. 4. Histogram of the results for the maximum change in length measured among the 3 principal body axes in each simulation. The most commonly measured maximum change in axis length was between 0.125 mm and 0.145 mm. The red dot shows the mean change in axis length, with error bars representing one standard deviation in the positive or negative directions. (For interpretation of the references to color in this figure legend, the reader is referred to the web version of this article.)

magnitude from $|\vec{L}| = |\hat{I}\vec{\omega}|$ where $\hat{I}$ is the inertia tensor and $\vec{\omega}$ is the angular (spin) frequency vector. We also note that the direction of the angular momentum vector does not change appreciably with respect to the spin vector over the course of the encounter, maintaining an angle of about 8° between them, and thus we use the spin frequency as an
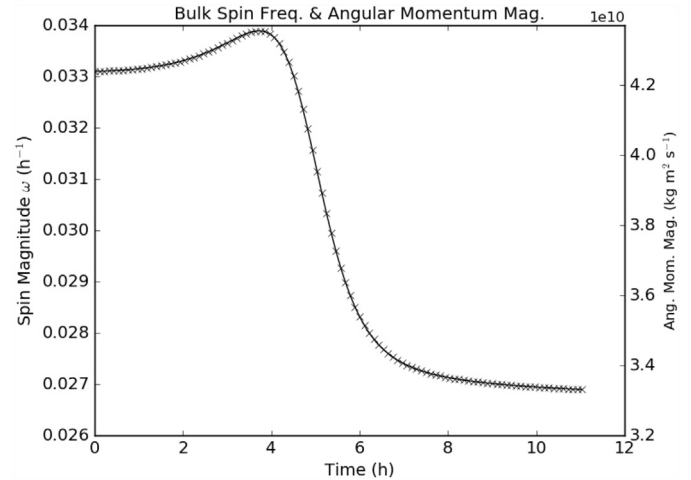

Fig. 5. Change in bulk spin magnitude (inverse of the period) and magnitude of the angular momentum vector for Apophis during the same simulation as shown in Fig. 3. Note that the evolution of the magnitude of the angular momentum vector is similar to the that of the spin frequency since the inertia tensor is essentially constant in the body frame during the encounter; the body does not appreciably change shape across the encounter. We also note that, for similar reasons, the direction of the angular momentum vector does not appreciably change over the course of the encounter; its direction relative to the direction of the spin axis maintains a value of ~**8°** through this encounter. Also notice that the spin rate of the object decreases by the end of the encounter and reaches a new equilibrium in that new spin state. While not all trials show a decrease (see Fig. 6), a new equilibrium spin is reached by the end of every simulation.

equivalent measure of the angular momentum in analyzing the change in spin state. One can see, in this example, that the spin frequency of the body follows the trend of a trailing-edge flyby, as described in Scheeres et al. (2000), such that the spin rate decreased as a result of the encounter. This result is not representative of all encounters, as the spin orientation at close approach varied widely with the differences in initial spin state, and signatures of leading-edge, trailing-edge, and end flybys (Scheeres et al., 2000; see their Fig. 9) were observed several times. In this and all other cases, Apophis' rotation state changes over the course of the encounter (even stabilizing on these timescales).

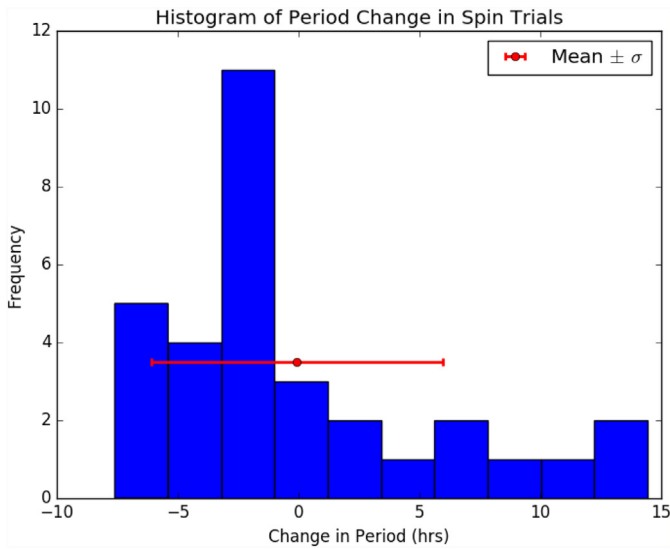The full results of the changes in the spin period of Apophis over the

Fig. 6. Histogram of results for the final change in bulk spin period for each encounter simulation. The most commonly measured final period change was between −1 h and − 3 h. The red dot shows the mean change in bulk spin period, with error bars representing one standard deviation in the positive or negative directions. The largest change represents a nearly 50% increase in the spin period of Apophis, but a negligible (close to 0 h) change is also a possible outcome. (For interpretation of the references to color in this figure legend, the reader is referred to the web version of this article.)

course of the encounter are shown in Fig. 6 and are summarized in Table 2. Note in Fig. 6 that, while the mean change in the spin period is close to 0 h, the statistic that perhaps better represents the changes seen in the bulk spin period may be the standard deviation, coming out to ± 6 h, indicating the large effect that the body orientation can have on the bulk spin period post-encounter. In some cases, the period of Apophis was increased by nearly 50%, but the most typical change to the spin period was a decrease by between 1 and 3 h. These results agree well with those found by Scheeres et al. (2005) for a rigid, tri-axial ellipsoid with axis length ratios of 1.4 between the major and intermediate axes and 0.8 between the minor and intermediate axes (see their Fig. 1).

3.3. Dependence on variable initial bulk densities

3.3.1. Axis length change

A suite of simulations across different bulk densities but at the same spin state (as described in Section 3.1) were also performed, to see the how trends for the changes in maximum axis length and rotation period across the encounter depend on bulk density.

Fig. 7 shows the trends in the maximum change in axis length (defined as above) across 18 varying-density trials separated into 3 different initial spin orientations and 6 different bulk densities at each orientation. The orientations were chosen randomly from among those used in the trials discussed in the previous section; we used three to get a representative sample, as it was too expensive to do this analysis for every initial spin orientation considered in Section 3.2. In random samples 2 (blue) and 3 (green), and for bulk densities > 2 g/cm^{-3}, we see that as the bulk density gets larger, the maximum strain along the axis decreases. The trend seen in the last set (red) shows the maximum axis length change increasing as the density increases from 3.1 g/cm^{-3} to 3.6 g/cm^{-3} — the opposite of the expected trend with increasing mass. Additionally, we note that there was a significantly larger strain for a density of 1.1 g/cm^{-3} in random sample 1, a trend which is not apparent in the other two data sets. Upon further inspection, we see that the orientation at perigee changes slightly as the bulk density increases, due to differences in the torques per unit mass acting on an
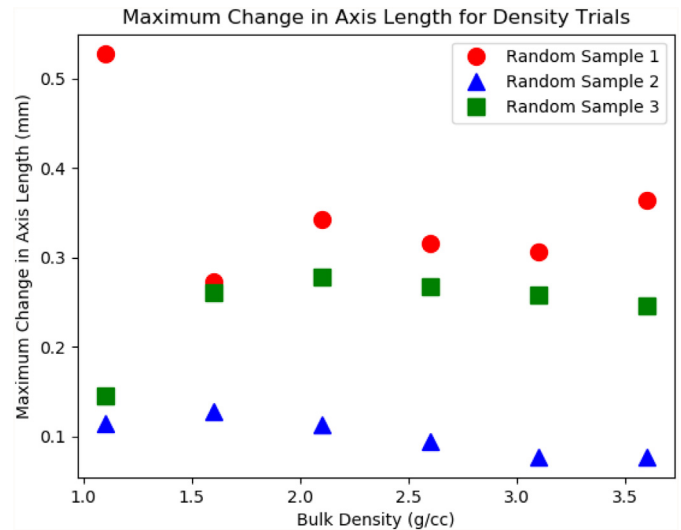

Fig. 7. Trends in the maximum change in axis length along the 3 primary body axes for different bulk density models of Apophis at 3 different initial spin orientations. Each color/shape identifies trials run with a specific spin orientation (randomly chosen from the orientations sampled in the 32 trials over varying spin states). See Section 4 for further discussion about the trends. (For interpretation of the references to color in this figure legend, the reader is referred to the web version of this article.)

Apophis model of higher mass (see Section 2.2.3). In the specific case represented by random sample 1 in Fig. 7, the principal axis experiencing the greatest acceleration is close to pointing parallel to the Earth at the time of perigee, thus causing larger variations in the strain along that axis, despite the increases in bulk density.

3.3.2. Period change

Fig. 8 shows the trends in the difference in final and initial bulk rotation periods across the encounter for the same 18 trials described above. In all three sets, for bulk densities > 2 g/cm^{-3}, we see the trend
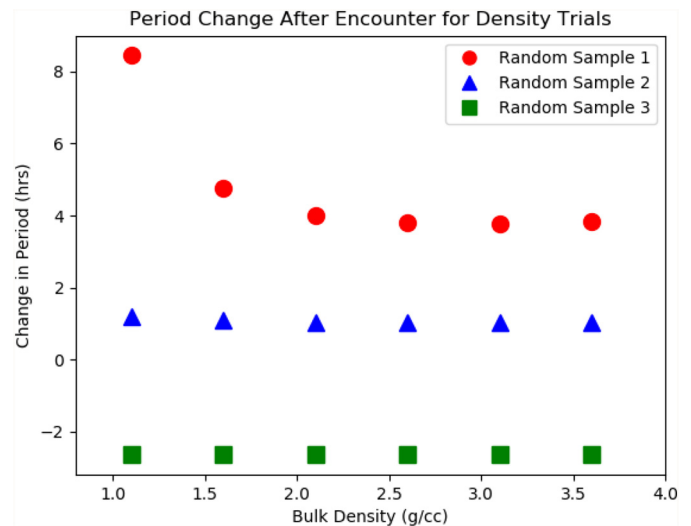

Fig. 8. Changes in the bulk spin period during 3 sets of simulations over varying bulk density with constant initial spin orientations. Note that, for each initial spin state, the trend for the change in spin period remains mostly constant (but very slightly decreases) with increasing bulk density. As in Fig. 7, the different colors/shapes refer to different initial spin orientations, chosen from the initial spin states sampled in the 32 trials over varying spin orientation at constant density. Non-conforming behavior for low-density cases is discussed in Section 4. (For interpretation of the references to color in this figure legend, the reader is referred to the web version of this article.)

of a nearly constant change in the bulk spin period across the encounter for each different density. This near constancy makes sense, as the moment arm barely changes for this range of bulk densities and choice of Young's modulus, and angular accelerations on a more massive body are expected to remain constant as well. In random sample 1, we expect that the slight changes in the body's orientation at perigee, due to the changing inertia tensor, as mentioned in Section 2.2.3, are causing larger variations at low densities in the post-encounter period change because the primary axis experiencing the greatest change is pointed closer to parallel with the Earth at the time of perigee.

3.4. Dependence on choice of Young's modulus

The final suite of simulations were made using a constant spin state and constant bulk density of $2.9\,\mathrm{g/cm^{-3}}$, but with a varying choice of Young's modulus, which directly relates to a different spring force between the particles. These simulations were performed in order to determine how the signal that we measure in the simulations scales with the Young's modulus of the body, as a higher material strength could dampen the strain signal measured. For these encounters, we chose Young's moduli ranging, by factors of 10, from 1 kPa to 1 MPa. The trend for these data is shown in Fig. 9.

Note, in Fig. 9, that the trends in the fit line show the maximum axis length change go to 0 as Young's modulus goes to infinity, meaning that an infinitely strong material will show no strain during the encounter, as expected. The trend as Young's modulus goes to 0 shows the maximum axis length change going to infinity, but this bound is limited by the breakup of the body: in cases of an asteroid with sufficiently low Young's modulus, the body will disassociate before reaching perigee. This relationship follows if the strain is directly proportional to the stress with the constant of proportionality being the Young's modulus. This seems to hold for the body as a whole, even though the contact
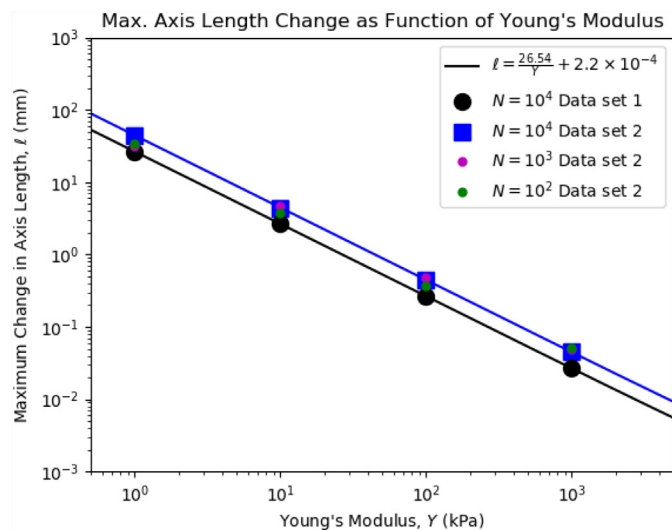

Fig. 9. Trends in the maximum change in axis length among the 3 primary body axes for different choices of Young's modulus and particle resolution. The lines represent fit lines through the data, described by equations of the form $\ell = \frac{m}{Y} + b$ where m is a fit parameter with units equivalent to a spring constant (e.g. $m = 26.54 \pm 0.001$ kPa mm for the black line), b is a fit parameter with units of length and is of order 0 (e.g. $(2.2 \pm 5.4) \times 10^{-4}$ mm for the black line), and ℓ and Y are the maximum axis length change during the encounter (mm) and Young's modulus (kPa), respectively. Trials with the same "data set" marking indicate the same initial spin state but different particle resolutions. The blue and black data sets have the same resolution ($N = 10^4$), but a different initial encounter orientation. Note that a Young's modulus a factor of 10 larger results in a signal strength almost exactly 10 times smaller. (For interpretation of the references to color in this figure legend, the reader is referred to the web version of this article.)
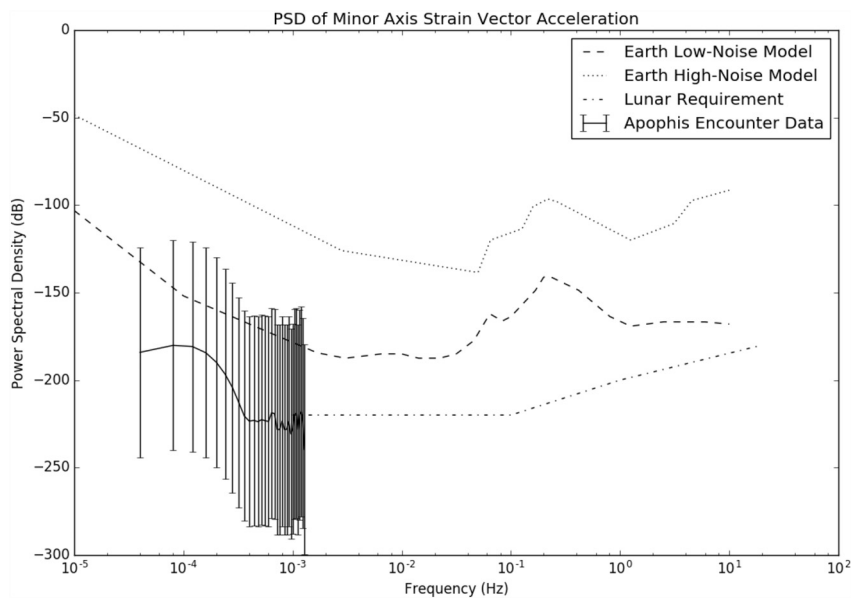
force law only operates between individual particles. We note that we only considered HCP configurations (see Section 2.2.1), so the dependence may be different for other internal particle configurations, which we will investigate in future work. Further, we note from this figure that particle resolution has little effect on the signal measured as long as the body is started with the same initial encounter orientation.

4. Discussion

We find, in our simulations, that the dependence on the bulk density of the maximum axis length change and change in spin period is small for bulk densities greater than or equal to about $1.6\,\mathrm{g/cm^{-3}}$. At the very lowest bulk densities tested, around $1.1\,\mathrm{g/cm^{-3}}$, we find that we may be approaching densities close enough to the Roche limit of the body that particularly strong encounter orientations can cause deviations from the behavior expected from higher density models. These results support our hypothesis that the orientation of Apophis at perigee, due to its rotational state, has a much larger effect on both the change in spin state and the expected strain during the encounter. As one can see in Fig. 8, the difference in period change between the first and last points of the red data set, marking the biggest difference between points with the same encounter orientation, is no larger than the difference between any given pair of points in the red and green data sets for the same density (for interpretation of colors, please see the web version of this article). Even looking at the results in Table 2, we see that the standard deviation among trials with different spin states ($\pm 6\,\mathrm{h}$) is much larger than the typical difference between points for trials with different densities and the same spin state ($< 1\,\mathrm{h}$). Similar arguments hold for the strain results. Furthermore, our results for the typical change in spin period based on encounter orientation (see Fig. 6) agree well with the results found in Scheeres et al. (2005).

In our simulations, we vary the bulk density of Apophis by scaling the mass of each particle at fixed particle radius, thereby maintaining the dimensions of the body but changing its total mass. In reality, the densities of the constituent grains that make up Apophis, assuming it is a rubble-pile and an S-type asteroid (Binzel et al., 2009), will all be in the region of 3.1 to $3.8\,\mathrm{g/cm^{-3}}$ (Flynn et al., 1999; Britt et al., 2002). The differences we model in bulk density should therefore come from the porosity of the body — void space between the constituent blocks and grains that make up its interior. This is seen in the case of Itokawa in that it, too, is an S-class asteroid (Binzel et al., 2001) and a rubble pile of bulk density $1.9\,\mathrm{g/cm^{-3}}$ with constituent grains having bulk density in the range specified above, but a bulk porosity of approximately 40% (Abe et al., 2006). This implies that the large changes to the mass of Apophis that are made in our simulations to sample different bulk densities and measure the effects of such changes should be interpreted carefully. Despite these caveats, our result regarding changes in bulk density having much smaller effects on the typical strain and spin change measured during the encounter give us confidence that the non-physical effects of our method of varying bulk density are minimal.

The remainder of our simulations shows that varying the Young's modulus of the constituent grains had a large effect on the strains measured. A factor of 10 difference in Young's modulus led to almost exactly a factor of 10 difference in maximum strain measured along one of the primary body axes. This shows that the Young's modulus, or material strength, of the regolith on the actual asteroid will have a significant effect on what types of seismic signals one could measure during the encounter with an in-situ seismometer or other device. We are able to characterize this dependence using the fit equation shown in Fig. 9. This fit shows that we can delineate an expected range for the strength of the strain signal, given a plausible range for the value of the Young's modulus. Since the Young's modulus of the material has the largest influence on the strength of the tidal encounter, plausible estimates of this parameter could provide a first-order constraint on the necessary sensitivity of an instrument attempting to measure the

Fig. 10. A comparison of the tidal-encounter-produced ground motion to seismic signal environments on the Earth and Moon. The Welch power spectral density is derived from the numerically calculated acceleration along the minor axis. This shows the maximum length change during our nominal tidal encounter. Also plotted are the high- and low-noise seismic models for the Earth (Peterson, 1993) and baseline requirement for a future lunar seismometer (Cohen et al., 2009). Error bars represent the range of behavior based on Young's modulus 10^3 (strongest signal) and 10^9 (weakest signal) Pa based on the typical trend shown in Fig. 9. The frequency used in the calculation of the Welch power spectral density was the length of one timestep ($\approx$ **6** min) in Hz.

strength of the strain signal on a potential mission to the body.

Using data from an encounter with a maximum axis length change close to the mean value we found across all of our trials, we determined the acceleration of the strain vector along the axis showing the maximum length change. The resulting acceleration is a low-frequency ground motion that could be detectable by a high-sensitivity, long-period seismometer placed on the surface of the asteroid. To determine how sensitive an instrument would need to be in order to observe the tidally induced ground motion, we plot the Welch power spectral density (PSD) of the acceleration of the strain vector along that axis next to the data for the high- and low-noise-models for the Earth (Peterson, 1993) and the lunar requirement based on seismic data from Moon missions (Cohen et al., 2009) in Fig. 10. We extend our previously investigated range of Young's modulus from 10^3 to 10^9 Pa and show this range as error bars in the PSD of the data. These data allow us to determine a baseline for the strength of the tidal seismic signals that an in-situ seismometer would be able to measure. We see in Fig. 10 that, for a typical Young's modulus around 1 MPa, the expected tidal seismic signal would be below the background noise floor on Earth. However, the predicted tidal signal is just above or near the projected background instrumental noise floor requirement determined for future instrumentation that would be deployed to the Moon (Cohen et al., 2009). Instrumentation developed for this next generation of space seismometers, such as those proposed in Schmerr et al. (2018), should have the sensitivity to measure low-frequency signals ($<$ 1 mHz) like those we predict. Detection of asteroid seismicity such as micrometeorite impacts or tidally induced disturbances (such as small surface landslides) would require seismometers that operate at much higher frequencies ($>$ 1 Hz).

Finally, we note the effect of the model resolution on the measured strain during the encounter. We see in Fig. 9 that, as the number of particles in the model increases (and thus the size of any given particle decreases), we see little change in the maximum strain. This makes sense based on our discussion in Section 2.2.2: since the spring constant is directly proportional to the particle size for a constant Young's modulus, we would expect little to no difference in measured strain for trials with lower resolutions and identical initial encounter orientations. We do expect that even with our best particle resolution, about 7 m in radius, small-scale granular effects occurring in particles of centimeter-size or less as predicted in Yu et al. (2014) are not observable. Our models with Young's modulus $Y = 10^6$ may also overestimate the strains during encounter due to the large uncertainties in determining a representative value for this number. This overestimate

may be mitigated, however, by our use of monodisperse spheres in an HCP configuration. HCP is the packing distribution that allows the least amount of void space between monodisperse spheres, meaning that the particles in our simulation are packed about as tightly as possible, and therefore HCP damps the signal by some amount. We know from images of Itokawa (Abe et al., 2006; Barnouin-Jha et al., 2008) that Apophis is likely composed of many $>$ 10,000 grains, that the grain size will likely vary from sandlike (micron scale) to boulders (meter scale), and that the constituent regolith will almost certainly not be packed in a perfect HCP configuration (since, at a minimum, grains are not likely to be spherical). In general, we expect that the HCP configuration has done more to damp the predicted strains from the encounter than other effects have done to amplify it. The results presented here, then, may actually be conservative estimates of the typical strains and spin changes that can be expected in the 2029 Apophis tidal encounter with the Earth (also see Yu et al., 2014).

5. Summary

In summary, these are the main results of our simulations:

- The expected maximum detectable strain is 0.133 $\pm$ 0.066 mm for a model of Apophis with bulk density 2.9 g/cm^{-3} and material parameters representative of terrestrial gravels/silts with a Young's modulus of 10^6 Pa.
- A deployed seismometer of appropriate sampling frequency ($< 10^{-3}$ Hz) and sensitivity (see Fig. 10) would be capable of detecting a strain signal of this magnitude over the length of time of the encounter (Schmerr et al., 2018).
- The expected change in the bulk rotation period of the same model of Apophis covers a wide range, up to a 50% increase or a 33% decrease for the cases examined. A change in spin state of this magnitude could change the Yarkovsky forces acting on the body, and thus change its post-encounter orbital solution. The factor that contributes the most to a change in the Yarkovsky forces, however, is the change in direction of the angular momentum vector, which is not measured here.
- The most significant factors in determining the maximum detectable strain or change in bulk rotation period are the material strength of the regolith on Apophis, and its orientation at perigee.
- The bulk density of Apophis has little effect, when compared to the perigee orientation or Young's modulus, on the maximum detectable strain or change in bulk rotation period for this particular encounter

scenario.

6. Future work

Some of the most interesting possible continuations of this work would be to perform a similar suite of simulations using a different packing distribution, a range of particle sizes, or both. We note above that HCP has the highest packing efficiency for monodisperse spheres, and therefore leaves the least void space in the body. In order to create a more realistic model of Apophis, one could generate a randomly packed particle distribution using polydisperse particle sizes. This different packing distribution would create the potential for more void space in the body and less regularity in the spacing among interior and exterior grains. Specifically, the body would likely have a lower shear strength, meaning it would be more deformable, and therefore one may see a larger strain signal. In addition, force chains will be more isotropic.

One could also investigate a model of Apophis as a collection of larger, rigid-aggregate cores covered by layers of regolith. This model is inspired by insights from Brozović et al. (2018), where their best-fit shape model, the one that was used for these simulations, resembles a contact binary, generated from two ellipsoidal components in contact. This scenario may affect the strain detected through the encounter because two larger boulders in contact are more easily detachable by tidal forces than a collection of loose grains (Richardson et al., 2005).

Acknowledgments

Appendix A. Estimate of expected strain

We examine a scenario with two identical, spherical particles in contact and find the difference in their equilibrium overlap distance, as described in Section 2.2.2, when they are in free space versus when they are under the influence of Earth's gravity, with the system's center of mass distance located at the nominal center of mass distance to Apophis at its 2029 perigee. The particles are aligned such that the axis through the particle centers also goes through the center of the Earth, so the maximum difference in tidal force is experienced and all vectors can be represented as acting in a positive or negative direction along this axis. The total gravitational force on each particle is the vector sum of the interparticle gravitational force and the tidal force felt from the Earth,

$$F_g^i = -\frac{Gm_i m_j}{r_p^2} + \frac{GM_E m_i}{r_i^2} \tag{A.1}$$

$$F_g^j = \frac{Gm_i m_j}{r_p^2} + \frac{GM_E m_j}{r_j^2} \tag{A.2}$$

where G is Newton's gravitational constant, $m_{i,j}$ represent the (identical) masses of the particles, M_E is the mass of the Earth, r_p is the distance between the particle centers, and $r_{i,j}$ are the distances of the respective particle centers from the Earth center, where particle i is closer to the Earth than particle j. When looking at the distances between the particle centers and the distances between particle-centers and Earth-center, we must be careful to account for the overlap between the particles resulting from the SSDEM implementation. We use particles with radius 7.14 m and mass density 3.94 g/cm^{-3}, as used in our simulations, thus with particle masses equal to 6.12×10^6 kg. We then calculate the difference in the gravitational forces acting on the particles, balance this difference in gravitational force with the restoring spring force from the SSDEM implementation, and solve for the change in the equilibrium particle position (Δx).

$$\Delta F_g = F_g^i - F_g^j \tag{A.3}$$

$$\Delta x = \frac{-\Delta F_g}{k_n} \tag{A.4}$$

We use the values of particle radii and spring constant defined in Section 2.

We calculate the perigee distance of Apophis (3.79×10^7 m) using the semimajor axis (-1.17×10^7 m) and eccentricity (4.25) from the updated ephemeris (Brozović et al., 2018). This calculation finds $\Delta x \approx 1$ µm (10^{-6} m): a reasonable value, considering the small masses of the particles and the large distances from the Earth.

Appendix B. Comparison of centrifugal and tidal accelerations

The true spin state of Apophis consists of tumbling motion with rotation and precession periods 263 ± 6 h and 27.38 ± 0.07 h, respectively, thus with a mean spin period of 30.56 ± 0.01 h (Pravec et al., 2014). In this investigation, we have assumed Apophis not to be in a tumbling state with changing centrifugal accelerations, but rather in a spin state with approximately the mean spin period about a randomly chosen spin axis from a set of plausible values (Section 2.2.3). Here, we show that the maximum difference between the strongest outward centrifugal acceleration, where Apophis is rotating with a period equivalent to its true precession period, and the centrifugal accelerations that we model by using the mean spin are negligible compared to the tidal accelerations experienced at perigee.

We first calculate the differential of the centrifugal acceleration with respect to the spin frequency:

$$\Delta a_c \approx 2\omega L \Delta \omega \tag{B.1}$$

Here, we use the mean spin frequency corresponding to a period of 30.56 h for ω and the difference in frequencies between ω and the frequency

---

[3] http://www.povray.org/.

corresponding to a period of 27.38 h for $\Delta\omega$. We also define L as the typical length scale of the body, about 200 m for the radius of the long axis. Using these values, we find that $\Delta a_c \approx 1 \times 10^{-7}$ m s^{-2}.

Next, we calculate the first order tidal acceleration felt at a perigee distance of 5.7 Earth radii, or 3.6×10^7 m:

$$\Delta a_t \approx \frac{2GML}{q^3} \qquad\qquad (B.2)$$

Here, we use the same length scale as before, the perigee distance q in meters, M as the Earth's mass in kg, and G in SI units. With these values, we find $\Delta a_t \approx 3 \times 10^{-6}$ m s^{-2}. Comparing this with the previous value, we see that the difference in the centrifugal acceleration in the worst case is about 3% of the tidal acceleration felt at perigee. We deem this small contribution to be negligible even in this extreme case when the body is rotating with period equal to the precession period. This means that the changing centrifugal accelerations due to the tumbling motion of the body will not make a significant difference in the strain signal measured due to the tidal accelerations.

References

Abe, S., Mukai, T., Hirata, N., Barnouin-Jha, O.S., Cheng, A.F., Demura, H., Gaskell, R.W., Hashimoto, T., Hiraoka, K., Honda, T., Kubota, T., Matsuoka, M., Mizuno, T., Nakamura, R., Scheeres, D.J., Yoshikawa, M., 2006. Mass and local topography measurements of Itokawa by Hayabusa. Science 312, 1344–1349.

Barnouin-Jha, O.S., Cheng, A.F., Mukai, T., Abe, S., Hirata, N., Nakamura, R., Gaskell, R.W., Saito, J., Clark, B.E., 2008. Small-scale topography of 25143 Itokawa from the Hayabusa laser altimeter. Icarus 198, 108–124.

Binzel, R.P., Rivkin, A.S., Bus, S.J., Sunshine, J.M., Burbine, T.H., 2001. Muses-c target asteroid (25143) 1998 sf36: a reddened ordinary chondrite. Meteorit. Planet. Sci. 36, 1167–1172.

Binzel, R.P., Rivkin, A.S., Thomas, C.A., Vernazza, P., Burbine, H.T., DeMeo, F.E., Bus, S.J., Tokunaga, A.T., Birlan, M., 2009. Spectral properties and composition of potentially hazardous asteroid (99942) Apophis. Icarus 200, 480–485.

Binzel, R.P., Morbidelli, A., Merouane, S., DeMeo, F.E., Birlan, M., Vernazza, P., Thomas, C.A., Rivkin, A.S., Bus, S.J., Tokunaga, A.T., 2010. Earth encounters as the origin of fresh surfaces on near-earth asteroids. Nature 463, 331–334.

Britt, D.T., Yeomans, D., Housen, K., Consolmagno, G., 2002. Asteroid density, porosity, and structure. In: Bottke Jr.W.F., Cellino, A., Paolicchi, P., Binzel, R.P. (Eds.), Asteroids III. University of Arizona Press, pp. 485–500.

Brozović, M., Benner, L.A.M., McMichael, J.G., Giorgini, J.D., Pravec, P., Scheirich, P., Magri, C., Busch, M.W., Jao, J.S., Lee, C.G., Snedeker, L.G., Silva, M.A., Slade, M.A., Semenov, B., Nolan, M.C., Taylor, P.A., HOwell, E.S., Lawrence, K.J., 2018. Goldstone and Arecibo radar observations of (99942) Apophis in 2012–2013. Icarus 300, 115–128.

Chau, K.T., Wong, R.H.C., Wu, J.J., 2002. Coefficient of restitution and rotational motions of rockfall impacts. Int. J. Rock Mech. Min. Sci. 39, 69–77.

Cohen, B., Veverka, J., Banerdt, B., Dombard, A., Elkins-Tanton, L., Grimm, R., Nakamura, Y., Neal, C., Plescia, J., Smrekar, S., Weiss, B., Morgan, T., McDougal, J., 2009. ILN Final Report. Technical Report. NASA.

Farnocchia, D., Chesley, S.R., Chodas, P.W., Micheli, M., Tholen, D.J., MIlani, A., Elliott, G.T., Bernardi, F., 2013. Yarkovsky-driven impact risk analysis for asteroid (99942) Apophis. Icarus 224, 192–200.

Flynn, G.J., Moore, L.B., Klöck, W., 1999. Density and porosity of stone meteorites: implications for the density, porosity, cratering, and collisional disruption of asteroids. Icarus 142, 97–105.

Fujiwara, A., Kawaguchi, J., Yeomans, D.K., Abe, M., Mukai, T., Okada, T., Saito, J., Yano, H., Yoshikawa, M., Scheeres, D.J., Barnouin-Jha, O., Cheng, A.F., Demura, H., Gaskell, R.W., Hirata, N., Ikeda, H., Kominato, T., Miyamoto, H., Nakamura, A.M., Nakamura, R., Sasaki, S., Uesugi, K., 2006. The rubble-pile asteroid Itokawa as observed by Hayabusa. Science 312, 1330–1334.

Miyamoto, H., Yano, H., Scheeres, D.J., Abe, S., Barnouin-Jha, O., Cheng, A.F., Demura, H., Gaskell, R.W., Hirata, N., Ishiguro, M., Michikami, T., Nakamura, A.M., Nakamura, R., Saito, J., Sasaki, S., 2007. Regolith migration and sorting on asteroid Itokawa. Science 316, 1011.

Möhlmann, D., Seidensticker, K.J., Fischer, H.H., Faber, C., Flandes, A., Knapmeyer, M., Krüger, H., Roll, R., Scholten, F., Thiel, K., Arnold, W., 2017. Compressive strength and elastic modulus at Agilkia on comet 67p/Churyumov-Gerasimenko derived from the sesame/casse touchdown signals. Icarus 303, 251–264.

Peterson, J.R., 1993. Observations and modeling seismic background noise. In: USGS Numbered Series. US Geological Surveypp. 94 number 93-322 in Open-File Report.

Pravec, P., Scheirich, P., Durech, J., Pollock, J., Kusnirák, P., Hornoch, K., Galád, A., Vokrouhlický, D., Harris, A.W., Jehin, E., Manfroid, J., Opitom, C., Gillon, M., Colas, F., Oey, J., Vrastil, J., Reichart, D., Ivarsen, K., Haislip, J., LaCluyze, A., 2014. The tumbling spin state of (99942) Apophis. Icarus 233, 48–60.

Press, W.H., Teukolsky, S.A., 1977. On formation of close binaries by two-body tidal capture. Astrophys. J. 213, 183–192.

Quillen, A.C., Kueter-Young, A., Frouard, J., Ragozzine, D., 2016. Tidal spin down rates of homogeneous triaxial viscoelastic bodies. MNRAS 463, 1543–1553.

Richardon, D.C., Quinn, T., Stadel, J., Lake, G., 2000. Direct large-scale n-body simulations of planetesimal dynamics. Icarus 143, 45–59.

Richardson, D.C., Bottke, W.F., Love, S.G., 1998. Tidal distortion and disruption of Earth-crossing asteroids. Icarus 134, 47–76.

Richardson, D.C., Leinhardt, Z.M., Melosh, H.J., Bottke Jr., W.F., Asphaug, E., 2002. Gravitational aggregates: evidence and evolution. In: Bottke Jr.W.F., Cellino, A., Paolicchi, P., Binzel, R.P. (Eds.), Asteroids III. University of Arizona Press, pp. 501–515.

Richardson, D.C., Elankumaran, P., Sanderson, R.E., 2005. Numerical experiments with rubble piles: equilibrium shapes and spins. Icarus 173, 349–361.

Saito, J., Miyamoto, H., Nakamura, R., Ishiguro, M., Michikami, T., Nakamura, A.M., Demura, H., Sasaki, S., Hirata, N., Honda, C., Yamamoto, A., Yokota, Y., Fuse, T., YOshida, F., Tholen, D.J., Gaskell, R.W., Hashimoto, T., Kubota, T., Higuchi, Y., Nakamura, T., Smith, P., Hiraoka, K., Honda, T., Kobayashi, S., Furuya, M., Matsumoto, N., Nemoto, E., Yukishita, A., Kitazato, K., Dermawan, B., Sogame, A., Terazono, J., Shinohara, C., Akiyama, H., 2006. Detailed images of asteroid 25143 Itokawa from Hayabusa. Science 312, 1341–1344.

Sánchez, P., Scheeres, D.J., 2011. Simulating Asteroid Rubble Piles with a Self-Gravitating Soft-Sphere Distinct Element Method Model. vol. 727. pp. 120.

Scheeres, D.J., 2001. Changes in rotational angular momentum due to gravitational interactions between two finite bodies. Celest. Mech. Dyn. Astron. 81, 39–44.

Scheeres, D.J., Ostro, S.J., Werner, R.A., Asphaug, E., Hudson, R.S., 2000. Effects of gravitational interactions on asteroid spin states. Icarus 147, 106–118.

Scheeres, D.J., Benner, L.A.M., Ostro, S.J., Rossi, A., Marzari, F., Washbaugh, P., 2005. Abrupt alteration of asteroid 2004 mn₄'s spin state during its 2029 Earth flyby. Icarus 178, 281–283.

Schmerr, N.C., Lekic, V., Mautino, A., Plescia, J.B., Paul, M., Richardson, D.C., Yu, H., DeMartini, J., 2018. The Asteroid Probe Experiment (Apex): Seismology at 99942 Apophis. Lpsc 2018, Poster.

Schwartz, S.R., P. M., Richardson, D.C., 2013. Numerically simulating impact disruptions of cohesive glass bead agglomerates using the soft-sphere discrete element method. Icarus 226, 67–76.

Schwartz, S.R., Richardson, D.C., Michel, P., 2012. An implementation of the soft-sphere discrete element method in a high-performance parallel gravity tree-code. Granul. Matter 14, 363–380.

Stadel, J., 2001. Cosmological N-Body Simulations and their Analysis. Ph.D. thesis. University of Washington.

Thuillet, F., Michel, P., Maurel, C., Ballouz, R.L., Zhang, Y., Richardson, D.C., Biele, J., Tatsumi, E., Sugita, S., 2018. Numerical modeling of lander interaction with a low-gravity asteroid regolith surface. In: Application to MASCOT on Board Hayabusa2. vol. 615. pp. A41.

Walsh, K.J., Richardson, D.C., 2008. A steady-state model of NEA binaries formed by tidal disruption of gravitational aggregates. Icarus 293, 553–566.

Walsh, K.J., Richardson, D.C., 2012. Spin-up of rubble-pile asteroids: disruption, satellite formation, and equilibrium shapes. Icarus 220, 514–529.

Yu, Y., Richardson, D.C., Michel, P., Schwartz, S.R., Ballouz, R.L., 2014. Numerical predictions of surface effects during the 2029 close approach of asteroid 99942 Apophis. Icarus 242, 82–96.

Zhang, Y., Richardson, D.C., Barnouin, O.S., Maurel, C., Michel, P., Schwartz, S.R., Ballouz, R.L., Benner, L.A.M., Naidu, S.P., Li, J., 2017. Creep stability of the proposed Aida mission target 65803 Didymos: I. Discrete cohesionless granular physics model. Icarus 294, 98–123.